

# Is Image-to-Image Translation the Panacea for Multimodal Image Registration? A Comparative Study

Jiahao Lu, Johan Öfverstedt, Joakim Lindblad\*, Nataša Sladoje

*MIDA Group, Department of Information Technology, Uppsala University, Uppsala, Sweden*

---

## Abstract

Despite current advancement in the field of biomedical image processing, propelled by the deep learning revolution, multimodal image registration, due to its several challenges, is still often performed manually by specialists. The recent success of image-to-image (I2I) translation in computer vision applications and its growing use in biomedical areas provide a tempting possibility of transforming the multimodal registration problem into a, potentially easier, monomodal one. We conduct an empirical study of the applicability of modern I2I translation methods for the task of multimodal biomedical image registration. We compare the performance of four Generative Adversarial Network (GAN)-based methods and one contrastive representation learning method, subsequently combined with two representative monomodal registration methods, to judge the effectiveness of modality translation for multimodal image registration. We evaluate these method combinations on three publicly available multimodal datasets of increasing difficulty, and compare with the performance of registration by Mutual Information maximisation and one modern data-specific multimodal registration method. Our results suggest that, although I2I translation may be helpful when the modalities to register are clearly correlated, registration of modalities which express distinctly different properties of the sample are not well handled by the I2I translation approach. When less information is shared between the modalities, the I2I translation methods struggle to provide good predictions, which impairs the registration performance. The evaluated representation learning method, which aims to find an in-between representation, manages better, and so does the Mutual Information maximisation approach. We share our complete experimental setup as open-source (<https://github.com/Noodles-321/Registration>), including method implementations, evaluation code, and all datasets, for further reproducing and benchmarking.

**Keywords:** image-to-image translation, generative models, biomedical image analysis, mutual information, neural style transfer, representation learning

---



---

\*Corresponding author

Email address: [joakim.lindblad@it.uu.se](mailto:joakim.lindblad@it.uu.se) (Joakim Lindblad)

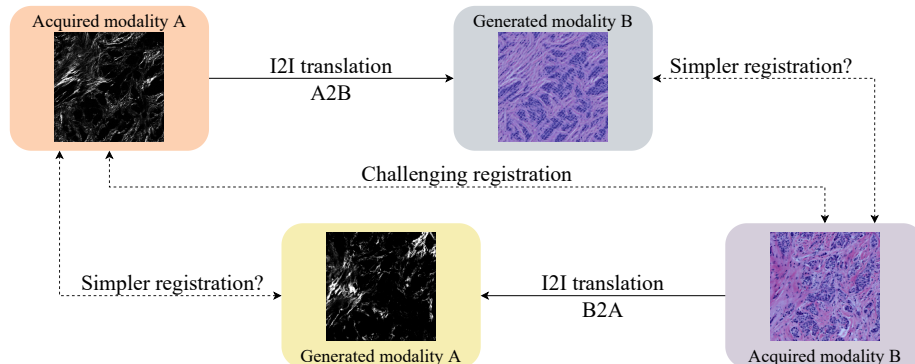


Figure 1: Method overview. Direct multimodal registration of distinctly different modalities is a challenging task (middle path). In this study, we evaluate if, instead, performing I2I translation of one modality to another may lead to a simpler monomodal registration problem (either of the two peripheral paths).

## 1. Introduction

We are witnessing a growing popularity of approaches which combine information from different imaging modalities [1] to maximise extracted information about an object of interest, particularly within life sciences. Different imaging techniques offer complementary information about structure, function, dynamics, and molecular composition of a sample. To efficiently utilise and fuse such heterogeneous information, acquired images have to be spatially aligned, a process known as image registration.

Numerous methods have been proposed for automatic monomodal (intra-modal) registration [2, 3, 4], typically based on comparison of intensity patterns in images (intensity-based approaches), or on finding correspondence between characteristic details in the images (feature-based methods). However, multimodal (intermodal) image registration is much more challenging. In cases when image appearances differ significantly between modalities, e.g., due to different underlying physical principles of imaging, assessing image similarity and finding correspondences across modalities are, in general, very difficult tasks.

Multimodal registration is often required and performed in medical and satellite imagery, where valuable information is in many situations acquired using several different sensors [5]. Due to the inherent discrepancy in intensity values in images acquired by different modalities, it is difficult to define generally applicable methods. Existing approaches are, therefore, often specific to a particular application (e.g., relying on anatomical properties of specific organs), and typically restricted to only a few combinations of modalities. Applications in biomedical image analysis bring in further challenges: (i) there exists a much greater variety of modalities (e.g., tens of different types of microscopies), (ii) specimens exhibit much wider variety, (iii) imaged objects (e.g., tissue) often lack distinctive structures (as opposed to, e.g., organs) which could be used

for establishing correspondences, (iv) acquired data often consists of very large images (easily reaching TB-size), necessitating fast methods with low memory requirements and also limiting the feasibility of high-quality manual annotation. Direct application of conventional methods is most often not sufficient, even in relatively simple scenarios. As a consequence, biomedical image registration is nowadays still often performed manually by specialists [6].

Deep learning-based methods have, since their renaissance, revolutionised the field of computer vision. Significant results with this type of methods have also been reached in the field of medical image registration, as summarised in recent surveys [6, 7, 8]. The main considered approaches include learning of similarity measures, direct prediction of transformation, and image-to-image (I2I) translation approaches. Generative Adversarial Network (GAN)-based methods have shown impressive performance in I2I translation tasks [9, 10, 11, 12, 13], offering the possibility of converting multimodal registration into a, presumably less challenging, monomodal problem which can be addressed by a wide range of monomodal registration methods; this idea is illustrated in Fig. 1. GAN-based approaches are receiving increasing attention in medical image registration [7, 8], and the progression to bioimage analysis seems to be a natural step. A recent survey [14] overviews several usage scenarios of GANs in the field of biomedical image analysis, primarily targeting data generation aiming to overcome challenges of annotation in digital pathology. However, results related to image registration, and particularly, in multimodal settings, are still lacking. The potential of GANs in these scenarios is still to be explored, as pointed out in a recent overview of the application of deep learning in bioimage analysis [15].

To fill this gap, and to facilitate knowledge transfer from the domains of natural and medical multimodal image registration, we present an empirical study of the applicability of modern I2I translation methods for the task of multimodal biomedical image registration. We compare the performance of four GAN-based methods, combined subsequently with two representative monomodal registration methods, to judge the effectiveness of modality translation on biomedical image registration. We evaluate these method combinations on three publicly available multimodal datasets. To explore the effects of different types of data and their complexity, w.r.t. the task of registration, we include one relatively easy non-biomedical dataset, one Cytological dataset of medium difficulty, and one more challenging Histological dataset. We include one classic intensity-based multimodal registration method, Mutual Information (MI) maximisation [16, 17], as a reference baseline. On the Histological dataset, we also compare with a recent task-specific method [18] developed particularly for that type of data. In addition, we evaluate one recently proposed deep learning-based method for multimodal registration which uses a different approach to transform multimodal registration into a monomodal case [19]. We share our complete experimental setup as open-source, including method implementations, evaluation code, and all datasets to facilitate further reproducing and benchmarking.

## 2. Background and related work

Image registration methodologies can roughly be classified into intensity-based and feature-based methods, however with no strict border between the two; several modern approaches estimate and align more or less dense feature fields, aiming to capture good properties of both intensity- and feature-based methods. Learning-based approaches may, to different extents, be utilised for directly solving the overall registration task (end-to-end), or for addressing different sub-tasks.

Intensity-based approaches typically formulate image registration as an optimisation problem, for which an image similarity measure (or inversely stated, a difference measure) is used to assess the quality of the alignment. Common similarity measures include negative Sum of Squared Differences (SSD) and Cross-Correlation (CC) for monomodal registration; Mutual Information (MI) [16] and Normalised Mutual Information [20] for both monomodal and multimodal registration; as well as measures which incorporate relevant additional information (e.g., gradient information or spatial displacement) extracted from the images [21, 22].

Several approaches for learning a suitable similarity measure have been proposed. A method to implicitly learn a multimodal similarity measure for the relatively easy multimodal scenario of registering T1 and T2-weighted Magnetic Resonance (MR) images is presented in [23], whereas [24] suggests training a Deep Convolutional Neural Network (DCNN) to predict correspondence of Computed Tomography and MR image patches and then use the classification score as a similarity measure.

Intensity-based approaches which rely on iterative local optimisation of an image similarity measure, are often relatively slow [8], and the existence of many local optima in the search space reduces applicability when the displacement between images to be registered is large [22]. Several learning-based approaches have been proposed to speed up the optimisation task; representative examples include VoxelMorph [25] and Quicksilver [23], where neural networks are used to improve the prediction of suitable steps in the optimisation.

Feature-based methods detect salient structures in the images and find correspondence between them, to guide the registration. Popular methods for feature point detection and description include SIFT [26] and ORB [27]. Learning may be utilised to suitably adapt feature-based registration to data. Pioneering unsupervised approaches for learning features for image registration are presented in [28] (for MR data) and [29] (natural scenes).

Compared to the iterative optimisation process of intensity-based methods, the feature-based approaches can be much faster and also more robust to variations in brightness and contrast, making this type of methods popular for computer vision and video tracking tasks. However, in multimodal setting, images typically convey complementary information; features that are present in one modality may be absent in another. Additionally, feature-based methods struggle with the general lack of salient structures in biomedical datasets. These shortcomings reduce the applicability of feature-based registration methods in



multimodal biomedical scenarios.

Modality Independent Neighbourhood Descriptor (MIND) [30] combines feature- and intensity-based notions and extracts a dense set of multi-dimensional descriptors of each of the images of different modalities, utilising the concept of self-similarity. A standard similarity-based (monomodal) registration framework is then used to establish correspondence between the generated representations.

Common representation of the images acquired by different modalities can also be learned; successful approaches include contrastive representation learning [19] and representation disentanglement [31]. Monomodal registration frameworks can then be applied to the resulting representations, as a suitable “middle ground” between the modalities.

I2I translation (also known as image style transfer) refers to mapping images from a source domain to a target domain, while preserving important content properties of the source image. I2I translation can be used to translate images from one modality into images appearing as if acquired in another modality. This enables transforming the multimodal registration problem into a, possibly easier, monomodal one, as illustrated in Fig. 1. I2I translation methods based on GANs [32] have, in recent years, shown impressive results [9, 10, 11, 12, 13].

I2I translation has found broad usage in biomedical areas [14], including virtual staining [33] stain style transfer [34], immunofluorescence marker inference [35], medical diagnosis [36, 37], surgical training [38]. Even though studies utilising I2I translation in multimodal registration exist, proposing to either directly align the translated images [39, 40] or indirectly incorporate the dissimilarity of modalities as a loss term in GANs [41, 42], their full potential, and in particular their application in biomedical multimodal image registration, are yet to be explored, as also pointed out by recent overviews [43, 44].

Unlike registration of medical images, e.g., brain [31, 45], cardiac [46], or whole-body [47], where methods can rely on the outline of shapes (organs), biomedical images rarely convey shape outlines, making automatic registration much more difficult. One recent example where the biological structural content has been used to align microscopy images is presented in [18]; this highly specialised method for registration of Second Harmonic Generation (SHG) and Brightfield (BF) images relies on a priori knowledge of the sample properties and the segmented image content.

### 3. Considered methods

We select four state-of-the-art GAN-based I2I translation methods and one representation learning method designed specifically for multimodal image registration. We subsequently combined these five methods with two monomodal registration approaches (one feature-based and one intensity-based).

#### 3.1. Reference methods

To provide reference performance, we include MI-based registration, as well as one special-purpose approach in our evaluation.

### 3.1.1. Maximisation of Mutual Information

The Mutual Information between images  $A$  and  $B$  is defined as

$$I(A, B) = \sum_{a \in \mathcal{A}} \sum_{b \in \mathcal{B}} p_{AB}(a, b) \log \left( \frac{p_{AB}(a, b)}{p_A(a)p_B(b)} \right) \quad (1)$$

where  $\mathcal{A}$  and  $\mathcal{B}$  denote the range of image  $A$  and  $B$  respectively,  $p_A(a)$  denotes the marginal probability of value  $a$  occurring in image  $A$ , and  $p_{AB}(a, b)$  denotes the joint probability of values  $a$  and  $b$  co-occurring in overlapping points of  $A$  and  $B$ . The probability mass functions  $p_A$ ,  $p_B$ , and  $p_{AB}$  can be estimated empirically as the normalised frequencies of image intensities and pairwise image intensities.

Intuitively, MI measures the information that is (pixelwise) shared between the images, and is high when the images  $A$  and  $B$  are well aligned. Maximisation of MI is widely used and has shown good performance in a number of multimodal registration tasks.

### 3.1.2. CurveAlign

*CurveAlign* is the first automatic registration method designed specifically to register BF and SHG images of whole tissue micro-array (TMA) cores [18]. The registration is based on the segmentation of the collagen structures in BF images, which are then utilised to guide the alignment with the corresponding structures in the SHG images, by maximising MI between the modalities. We include this method in the evaluation performed on the considered Histological dataset (Sect. 4.3).

## 3.2. Image-to-Image translation methods

### 3.2.1. pix2pix [9]

pix2pix provides a general-purpose solution for I2I translation utilising conditional GANs (cGANs) [48], which use aligned image pairs during training. pix2pix consists of a generator  $G$  and a discriminator  $D$  which are trained in an adversarial manner: the generator  $G$  is trained to generate fake images that cannot be distinguished from real ones by  $D$ , and  $D$  is trained to best separate the fake and the real images. The objective function is:

$$G^* = \arg \min_G \max_D \mathcal{L}_{cGAN}(G, D) + \lambda \mathcal{L}_{L1}(G), \quad (2)$$

where the cGAN loss  $\mathcal{L}_{cGAN}$  is to be minimised by  $G$  and maximised by  $D$  during training, and the pixel-wise regression loss  $\mathcal{L}_{L1}$  aims to make the output images closer to the ground truth. Based on the assumption that the structures in one image should be roughly aligned between the input and output, the architecture of the generator  $G$  is designed in a ‘‘U-Net’’ style [49].

pix2pix is included in our evaluation not only because of its pioneering role in the field, but also because it is regarded as a strong baseline framework [50, 51].

### 3.2.2. CycleGAN [10]

Using cycle-consistency constraint has been shown to be an effective approach to overcome the need for aligned image pairs during training [52]. Cycle-consistent adversarial network (CycleGAN) is a well-known representative of this approach [53, 54]. Its modified version has shown satisfying performance on the biomedical task of robust tissue segmentation [55] through stain transformation. Further modifications have also shown successes in other biomedical applications [37, 38]. The option of unsupervised training of CycleGANs makes them very attractive in biomedical applications.

The main idea behind CycleGANs is to enforce the image translation to be “cycle-consistent”, i.e., if an image is translated from domain  $X$  to  $Y$  and then inversely translated from  $Y$  to  $X$ , the output should be the same as the original image. To achieve this property, another generator  $F : Y \rightarrow X$  is introduced to couple with  $G$  such that  $G$  and  $F$  should be inverse mappings of each other. The used loss function combines two kinds of loss terms: the adversarial loss  $\mathcal{L}_{\text{GAN}}$  to encourage the mapped domain to be close enough to the target [32], and the cycle-consistency loss  $\mathcal{L}_{\text{cyc}}$  to enforce the invertibility of the mapping.

### 3.2.3. DRIT++ [13]

Aiming for more diverse output from a single input, DRIT++ is a recently proposed GAN of higher complexity, that performs unsupervised I2I translation via disentangled representations. More specifically, DRIT++ learns to encode the input image into a domain-invariant content representation and a domain-specific attribute representation in latent spaces. The domain-invariant content representation captures the information that the two domains have in common, while the domain-specific attribute representation captures the typical features in each domain. The output images are then synthesised by combining the disentangled representations.

For an I2I translation task across domains  $\mathcal{X}$  and  $\mathcal{Y}$ , the framework of DRIT++ is comprised of a content encoder  $E^c$ , an attribute encoder  $E^a$ , a generator  $G$  and a domain discriminator  $D$  for each domain respectively, and a content discriminator  $D^c$ . To achieve the intended disentanglement of information, the weights between the last layer of  $E_{\mathcal{X}}^c$  and  $E_{\mathcal{Y}}^c$  and the first layer of  $G_{\mathcal{X}}$  and  $G_{\mathcal{Y}}$  are shared, following the assumption that the two images share some information in a common latent space [56]. The content encoders  $\{E_{\mathcal{X}}^c, E_{\mathcal{Y}}^c\}$  are trained to make the encoded contents of the two domains indistinguishable from each other by the adversarial content discriminator  $D^c$ . DRIT++ also uses cross-cycle consistency loss, domain adversarial loss, self-reconstruction loss, and latent regression loss to encourage better quality of the generated images.

DRIT++ is included in this study because of its explicit extraction of shared information from the domains into a common latent space, notwithstanding its different purpose for output diversity, is highly in accord with what is required for image registration and may therefore conceptually be likely to lead to good performance.

#### 3.2.4. *StarGAN-v2* [11]

StarGAN-v2 is recently proposed to not only generate diverse output images, but also address the scalability to multiple domains. StarGAN-v2 comprises four modules: a style encoder  $E_y$  to extract the style code  $s = E_y(x_{\text{ref}})$  from a reference image  $x_{\text{ref}}$ , or alternatively, a mapping network  $F_y$  to generate a style code  $s = F_y(\mathbf{z})$  from an arbitrarily sampled vector  $\mathbf{z}$  in the latent space; a generator  $G$  to translate an input image  $x$  and a domain-specific style  $s$  into an output image  $G(x, s)$ ; and a multi-task discriminator  $D$  with multiple output branches  $D_y$  to classify whether an output image is real or fake for each domain  $y$ . In addition to the diversity loss  $\mathcal{L}_{\text{ds}}$  that enforces  $G$  to discover meaningful style features from the image space, it also uses cycle-consistency loss  $\mathcal{L}_{\text{cyc}}$  to preserve the content of the input image, style reconstruction loss  $\mathcal{L}_{\text{sty}}$  and adversarial loss  $\mathcal{L}_{\text{adv}}$  to ensure the output quality.

StarGAN-v2 is of specific interest due to the reported remarkably good visual quality of the generated images compared to the baseline models [57, 13], as well as the framework’s increasing popularity in the community. Its ability to inject domain-specific style into a given input image could potentially simplify the registration problem when more than two modalities are considered.

#### 3.2.5. *CoMIR* [19]

CoMIR is a recently proposed representation learning method that produces rotation equivariant image representations (typically of the same size as the input images), using an objective function based on noise-contrastive estimation (InfoNCE) [58]. Given a batch of image pairs, the images of each modality are transformed using DCNNs (one model per modality, without weight-sharing) to a learned embedding space. The objective function serves to train the models to generate similar mappings for the paired images, while generating dissimilar mappings compared to all the other images in the batch. CoMIR requires pairs of aligned images for its training procedure, similarly to pix2pix. One advantage of the approach taken by CoMIR is that the requirement is not to learn to reproduce the appearance of either modality, but rather to learn a representation of the content (signal) present in both modalities, mapping corresponding image pairs into images with similar structure and appearance.

Combined with a monomodal registration framework which is applied to the learned representations, CoMIR has shown to exhibit good performance in the registration of multimodal images [19]. It is included in this study as a reference method based on a modality translation approach alternative to I2I.

### 3.3. *Monomodal registration*

#### 3.3.1. *SIFT-based registration*

Scale-invariant feature transform (SIFT) [26], is a feature detector and descriptor invariant to affine transformations and robust to changes in illumination and partial occlusion. It has found wide usage in a range of image matching and object recognition applications. Due to its popularity and generally good performance, SIFT is included in this study and evaluated (in combination with

a suitable feature point matching and transformation estimation) on the original and generated images and their representations. The primary interest is in its performance in the (generated) monomodal scenarios.

### 3.3.2. Registration based on $\alpha$ -AMD

A monomodal image registration method based on iterative gradient descent optimisation of  $\alpha$ -AMD has shown very good and robust performance [59, 22]. The properties of  $\alpha$ -AMD, a symmetric distance measure between images which combines intensity and spatial information, enable to achieve a larger convergence region around the global optimum than commonly used similarity measures that are based on statistics or intensity differences of overlapping points. Registration based on minimisation of  $\alpha$ -AMD has been successfully applied in a variety of monomodal scenarios [22, 19, 60], which motivates our decision to include it in this study for the registration of the generated monomodal image pairs.

## 4. Data

We use three publicly available datasets in this study, to illustrate different applications (aerial, cytological, and histological imaging), combining different imaging modalities (Near-Infrared and RGB, Quantitative Phase Imaging and Fluorescence Microscopy, and finally Second Harmonic Generation Microscopy and Bright Field Imaging) and introducing different levels of difficulty of image registration (low, medium, and high).

### 4.1. Zurich data

The Zurich dataset comprises 20 QuickBird-acquired images (with side lengths ranging from 622 to 1830  $px$ ) of the city of Zurich [61]<sup>1</sup>. Each image is composed of 4 channels, Near-Infrared (NIR), and three colour channels (R,G,B). Each channel is globally re-scaled to the range [0, 255]. The NIR channel is extracted as Modality A (Fig. 2a), and the R-G-B channels are extracted jointly as Modality B (Fig. 2b).

### 4.2. Cytological data

The Cytological dataset is composed of correlative time-lapse Quantitative Phase Images (QPI)<sup>2</sup> and Fluorescence Images<sup>3</sup> of prostatic cell lines acquired by the multimodal holographic microscope Q-PHASE (TESCAN, Brno, Czech Republic) [62, 63]. Three cell lines (DU-145, PNT1A, LNCaP) are exposed to cell death-inducing compounds (staurosporine, doxorubicin, and black phosphorus) and captured at 7 different fields of view. The data consist of time-lapse stacks of several hundred 600×600  $px$  TIFF frames. Pixel values in the frames represent cell dry mass density in  $pg/\mu m^2$  in QPI images, and the amount of caspase-3/7

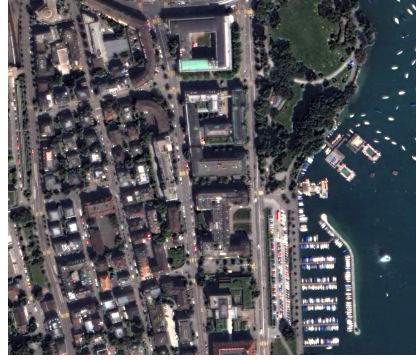
<sup>1</sup><https://sites.google.com/site/michelevolpfiresearch/data/zurich-dataset>

<sup>2</sup><https://zenodo.org/record/2601562>

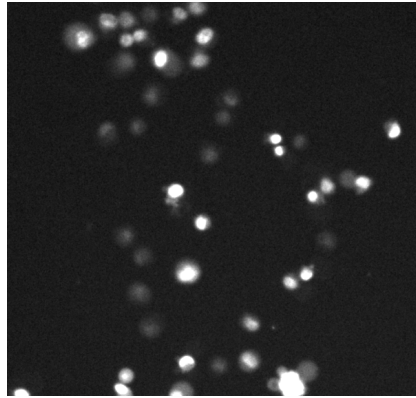
<sup>3</sup><https://zenodo.org/record/4531900>



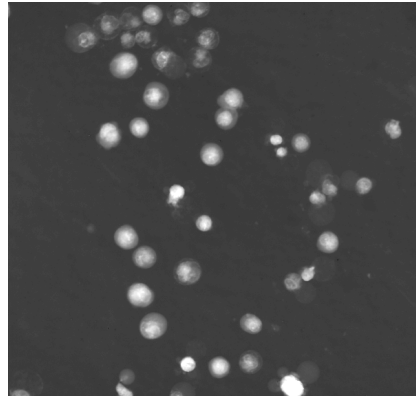
(a) Zurich dataset: Modality A



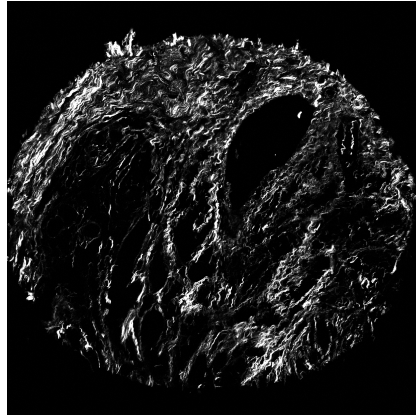
(b) Zurich dataset: Modality B



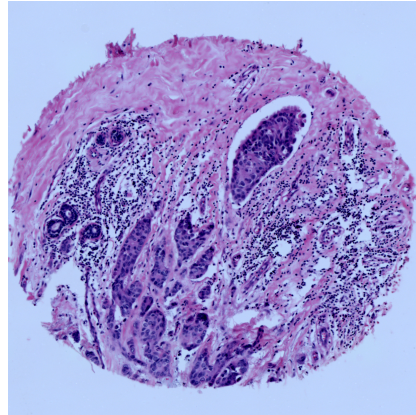
(c) Cytological data: Modality A



(d) Cytological data: Modality B



(e) Histological data: Modality A



(f) Histological data: Modality B

Figure 2: Examples of pairs of original images acquired by different modalities considered in this study (contrast enhanced for visualisation). Zurich dataset (aerial imaging): (a) NIR, (b) RGB; Cytological data: (c) Fluorescence microscopy, (d) QPI; Histological data: (e) SHG, (f) BF.

product accumulation in the fluorescence images (visualised using FITC 488 nm filter) [64]. For each time-lapse stack, the intensity values are globally re-scaled to the range  $[0, 255]$ . Frames with indices 0, 15, 30, 45, 60 backwards from the last are extracted. We use the fluorescence images indicating the caspase-3/7 level as Modality A (Fig. 2c) and corresponding QPI images as Modality B (Fig. 2d).

#### 4.3. Histological data

The Histological dataset comprises 206 aligned Second Harmonic Generation (SHG) and Bright-Field (BF) tissue micro-array (TMA) image pairs of size  $2048 \times 2048$  *px* [65]<sup>4</sup>. The tissue sections are from patients with breast cancer, pancreatic cancer, and kidney cancer. BF images are acquired using an Aperio CS2 Digital Pathology Scanner (Leica Biosystems, Wetzlar, Germany) at  $40\times$  magnification. SHG images are acquired using a custom-built integrated SHG/BF imaging system described in [18]. Each SHG-BF image pair is registered by aligning manually marked landmark pairs. SHG and BF images are referred to as Modality A (Fig. 2e) and B (Fig. 2f) of the Histological dataset, respectively.

#### 4.4. Ground truth alignment of the image pairs

Alignment of multimodal image pairs is, in general, a very difficult task, for a human, as well as for an automated system, which makes it challenging to create ground truth data required for benchmarking, as well as for training the registration algorithms. Hybrid imaging – simultaneous acquisition of images of a sample (or a scene) by more than one modality – may provide such aligned pairs directly. Hybrid imaging is, however, available only to a limited extent. The Zurich and Cytological dataset are acquired by hybrid imaging, while aligned pairs of the Histological images are, as mentioned, generated semi-automatically.

## 5. Experiments

### 5.1. Implementation of learning-based modality transfer methods

Aiming for a fair comparison, we use the same data augmentation for all the learning-based methods. For each dataset, 5120 square non-rotated patches of size  $362 \times 362$  *px* are randomly cropped from the training set. All models are trained with on-the-fly augmentation on top of the sampled patches. The augmentation includes, in a sequence: random horizontal flip ( $p = 0.5$ ); random rotation ( $\theta \in [-180, 180^\circ]$ ) using either ( $p = 0.33$ ) nearest neighbour, linear, or cubic interpolation; random Gaussian blur ( $p = 0.5$ ) with a standard deviation  $\sigma \in [0, 2.0]$ ; and centre-crop to size  $256 \times 256$  *px* (thus, no padding required).

Apart from the shared augmentation, we make as few changes as possible compared to the default settings of the respective official released codes<sup>5,6,7,8</sup>.

<sup>4</sup><https://zenodo.org/record/4550300>

<sup>5</sup><https://github.com/junyanz/pytorch-CycleGAN-and-pix2pix>

<sup>6</sup><https://github.com/HsinYingLee/DRIT>

<sup>7</sup><https://github.com/clovaai/stargan-v2>

<sup>8</sup><https://github.com/MIDA-group/CoMIR>

The following minor changes are applied to the original implementations: (i) mini-batch sizes are maximised under the limitation of 12 GB GPU memory, i.e., 8 for CoMIR, 64 for pix2pix and DRIT++, 4 for CycleGAN and StarGANv2; (ii) DRIT++ is set to use feature-wise transformation to enable shape variation on the Cytological and Histological data, but not on the Zurich dataset.

During inference, to fit the network architectures of pix2pix, CycleGAN and StarGANv2, input image sizes are padded to minimum multiples of 256 pixels using “reflect” mode to reduce artefacts, e.g., the input image size  $834 \times 834 px$  of Histological data is padded to  $1024 \times 1024 px$ . The padded areas of the images resulting from translation are cropped off before further processing. For DRIT++, to fit the image registration context, a modified version of the guided translation is used; instead of using the disentangled attribute representation of a random image from the other modality, the generator uses the disentangled attribute representation of the image that the current image is to be registered with. Similarly for StarGANv2, the style code of the reference image guiding the translation comes from the corresponding image in the target modality. Due to the restriction imposed by StarGANv2’s architecture that the reference image can only be of size  $256 \times 256 px$ , only the central areas of reference images are used to extract style code, to avoid resolution mismatch with training.

## 5.2. Implementation of image registration methods

All the used registration methods, except CurveAlign, expect greyscale data. RGB images (Modality B of Zurich and the Histological dataset) are therefore converted to greyscale, using  $L = 0.299R + 0.587G + 0.114B$ , before registration.

### 5.2.1. Iterative registration by Mutual Information maximisation

MI-based registration is performed using *SimpleElastix*<sup>9</sup> – an industry-standard image registration library [66]. Adaptive stochastic gradient descent (ASGD) [67] is used as the optimiser and the maximum number of iterations is set to 1024. To avoid local minima, a multi-resolution strategy with a 4-level Gaussian scale space is used for both Zurich and Cytological data, while 6 levels are used for Histological data, considering the larger image size.

### 5.2.2. SIFT feature detecting and matching

SIFT feature detector is implemented using *OpenCV*<sup>10</sup> [68]. The maximal number of retained feature points is limited to 500. Brute-force matching with cross-check is used to produce the best matches with the minimal number of outliers when there are enough matches. Other parameters remain at default settings. The rigid transformation between the two sets of matched coordinates is estimated using RANdom SAmple Consensus (RANSAC) algorithm [69] via the implementation in *scikit-image*<sup>11</sup> [70]. A data point is considered an inlier if

<sup>9</sup><https://simpleelastix.github.io>

<sup>10</sup><https://opencv.org>

<sup>11</sup><https://scikit-image.org/docs/stable/api/skimimage.measure.html#skimimage.measure.ransac>



its residuals calculated for the estimated model is smaller than  $2\text{ px}$ . For each image pair, the random sample selection procedure is iterated 100 times, and the final model is estimated using all inliers of the best model resulting from the performed iterations.

#### 5.2.3. $\alpha$ -AMD

$\alpha$ -AMD is implemented based on the *Py-Alpha-AMD Registration Framework*<sup>12</sup>. The following modifications are made compared to the settings in the example script: (i) Three resolution levels are used in a pyramid (coarse-to-fine) registration strategy, with sub-sampling factors set to (4, 2, 1) and Gaussian blur  $\sigma$  set to (12.0, 5.0, 1.0). The numbers of iterations per level are set to (900, 300, 60) for Zurich and Cytological data and to (3000, 1000, 200) for the larger Histological data; (ii) Three rotation, 0 and  $\pm 0.4$  radians, are used as starting points. After performed iterations, the transformation with the lowest distance is selected as the final registration output; (iii) Stochastic gradient descent (SGD) with momentum  $\alpha = 0.9$  and a sampling fraction 0.01 is used. Step sizes for the first two resolution levels are set to 2, while decreasing linearly from 2 to 0.2 for the last resolution level.

#### 5.2.4. *CurveAlign*

The used implementation of *CurveAlign*<sup>13</sup> follows the default settings in its V4.0 Beta version, except for restricting its default affine transformation to rigid.

### 5.3. Evaluation

Our main objective is to evaluate the success of registration of multimodal images, utilising images translated from one modality to another as an intermediate result (to which monomodal registration is applied). We find it relevant to also evaluate the performance of the I2I translation methods on the observed datasets, and explore the effect of the quality of modality translation on the success of subsequent registration.

#### 5.3.1. Evaluation sets

The Zurich dataset is divided into 3 sub-groups, enabling 3-folded cross-validation. The three groups are formed of the images with IDs: {7, 9, 20, 3, 15, 18}, {10, 1, 13, 4, 11, 6, 16}, {14, 8, 17, 5, 19, 12, 2}. Since the images vary in size, each image is subdivided into the maximal number of equal-sized non-overlapping regions such that each region can contain exactly one  $300 \times 300\text{ px}$  image patch, and then extracting one  $300 \times 300\text{ px}$  image patch from the centre of each region. The particular 3-folded grouping followed by splitting leads to that each evaluation fold contains 72 test samples.

The Cytological data contains images from 3 different cell lines; we use all images from one cell line as one fold in 3-folded cross-validation. Each image in

<sup>12</sup>[https://github.com/MIDA-group/py\\_alpha\\_amd\\_release](https://github.com/MIDA-group/py_alpha_amd_release)

<sup>13</sup><https://eliceirilab.org/software/curvealign>

the dataset is subdivided from  $600 \times 600 px$  into  $2 \times 2$  patches of size  $300 \times 300 px$ , so that there are 420 test samples in each evaluation fold.

For the Histological data, to avoid too easy registration relying on the circular border of the TMA cores, the evaluation images are created by cutting  $834 \times 834 px$  patches from the centre of the original 134 TMA image pairs.

The evaluation set created from each of the three observed image datasets consists of images undergone uniformly-distributed rigid transformations of increasing sizes of displacement. Each image patch is randomly rotated by an angle  $\theta \in [-20, 20]$  degrees (with bi-linear interpolation), followed by translations in  $x$  and  $y$  directions by  $t_x$  and  $t_y$  pixels respectively, where  $t_x$  and  $t_y$  are randomly sampled within  $[-28, 28]$  for Zurich and Cytological data, and within  $[-80, 80]$  for the Histological data. To minimise border artefacts, the transformed patches are, for Zurich and Cytological data, padded using “reflect” mode, or, for Histological data, cropped at the appropriate position directly from the original larger images.

Our created *Datasets for Evaluation of Multimodal Image Registration* is released on Zenodo with open access<sup>14</sup>. In total, it contains 864 image pairs created from the Zurich dataset, 5040 image pairs created from the Cytological dataset, and 536 image pairs created from the Histological dataset. Each image pair consists of a reference patch  $I^{\text{Ref}}$  and its corresponding initial transformed patch  $I^{\text{init}}$  in both modalities, along with the ground truth transformation parameters to recover the transformation. Scripts to compute the registration performance, to plot the overall results, and to generate more evaluation data with different setting are also included.

### 5.3.2. Metrics

**Modality translation:** Fréchet Inception Distance (FID) [71], a measure of similarity between two sets of images, has been widely used as an objective metric to assess the quality of GAN-generated images and has shown a high correlation with the subjective human judgement [13, 11, 44]. Lower FID (being a distance measure) indicates higher similarity of the images, i.e., higher quality of the image translation. We use a PyTorch implementation<sup>15</sup> of FID to evaluate the quality of images generated by the considered modality translation methods.

**Registration:** We evaluate the performance of the considered registration approaches in terms of their success in recovering rigid transformations of varying size applied to (one of the images in) the aligned pairs. To quantify the success of registration, we define the spatial distance  $D(I^1, I^2)$  between two image patches  $I^1$  and  $I^2$  as

$$D(I^1, I^2) = \frac{1}{4} \sum_{i=1}^4 \|C_i^2 - C_i^1\|_2, \quad (3)$$

where  $C_i^1$  and  $C_i^2$  respectively denote positions of the 4 corner points of  $I^1$  and

<sup>14</sup><https://zenodo.org/record/4587903>

<sup>15</sup><https://github.com/mseitzer/pytorch-fid>

Table 1: Success of modality translation methods expressed in terms of Fréchet Inception Distance (FID). Smaller is better. Standard deviations are taken over the 3 folds for Zurich and Cytological data. `cyc`, `drit`, `p2p`, `star`, `comir` denote the methods CycleGAN, DRIT++, pix2pix, StarGANv2, and CoMIR, respectively. Suffix `_A` (resp. `_B`) denotes generated Modality A (resp. B). The best result achieved by an I2I translation method on each of the datasets is bolded. FID between the generated CoMIR representations, as well as the initial FID between the considered multimodal image datasets (`B2A`), are included as a reference.

Method \ Dataset	Zurich Data	Cytological Data	Histological Data
<code>cyc_A</code>	232.4 $\pm$ 69.7	<b>35.1 <math>\pm</math> 11.9</b>	433.4
<code>cyc_B</code>	<b>91.5 <math>\pm</math> 27.0</b>	65.4 $\pm$ 16.9	156.1
<code>drit_A</code>	182.9 $\pm$ 3.3	63.1 $\pm$ 17.4	125.3
<code>drit_B</code>	144.1 $\pm$ 9.1	192.3 $\pm$ 50.4	123.7
<code>p2p_A</code>	93.7 $\pm$ 4.6	61.8 $\pm$ 18.5	<b>116.8</b>
<code>p2p_B</code>	94.4 $\pm$ 3.3	169.3 $\pm$ 6.9	153.0
<code>star_A</code>	165.5 $\pm$ 10.6	99.1 $\pm$ 53.5	174.2
<code>star_B</code>	135.6 $\pm$ 21.5	140.6 $\pm$ 24.4	142.7
<code>comir</code>	17.7 $\pm$ 8.0	61.5 $\pm$ 11.1	91.0
<code>B2A</code>	155.3 $\pm$ 15.4	145.0 $\pm$ 17.6	341.0

$I^2$ , when mapped into a common coordinate system.

The *initial displacement*  $d_{\text{Init}}$  of a synthetic transformation is the distance between a reference patch  $I^{\text{Ref}}$  and its corresponding initial transformed patch  $I^{\text{Init}}$ :  $d_{\text{Init}} = D(I^{\text{Ref}}, I^{\text{Init}})$ . The *absolute registration error*  $\varepsilon$  is the distance between the reference patch  $I^{\text{Ref}}$  and the transformed patch after registration  $I^{\text{Reg}}$ :  $\varepsilon = D(I^{\text{Ref}}, I^{\text{Reg}})$ . The *relative registration error*  $\delta$  is calculated as the percentage of absolute error to the width and height of the image patches:  $\delta = (\varepsilon/w) \times 100\%$ , with  $w = 300\text{ px}$  for Zurich and Cytological data, and  $w = 834\text{ px}$  for Histological data. To summarise the competence of the registration of a sample, it is considered successful when the relative registration error  $\delta < 2\%$ . The success rate  $\lambda$  is calculated as the ratio of succeed cases to total cases.

## 6. Results

### 6.1. Performance of the modality translation methods

To summarise the modality translation performance, we present in Table 1 the computed FID values measured on the three datasets, for modality translations performed by each of the four I2I translation methods, in two directions (A to B, and B to A). The values in a row `method_A` indicate the distance between the distribution of images in the `method`-generated Modality A, and of those in the real Modality A.

We observe that the FID values reflect: (i) different levels of asymmetry of the I2I translation methods in treating translations in one, or the other directions (e.g., `cyc`, compared to `p2p` on Zurich dataset); (ii) a consensus of all the methods that generation of Modality A of the Cytological dataset is considerably easier (i.e., more successful) than of Modality B; (iii) rather varying stability of the

results for the different methods, and the different datasets, as indicated by the large spread of standard deviations.

FID is also computed for CoMIR, indicating the difference between the distributions of the *representations* generated from Modality A and B. Although not directly comparable with the other values (computed on a rather different type of representation), these FID values, increasing from Zurich to the Histological dataset, are still informative in reflecting an increase in dataset difficulty.

Finally, the FID values in the row **B2A** indicate the difference between the original acquired multimodal images, for each of the three datasets. They can be seen as a reference value of the dissimilarity (FID) of the original images that, ultimately, are to be registered. We note that in some cases FID becomes higher after modality translation, compared to the initial **B2A** value.

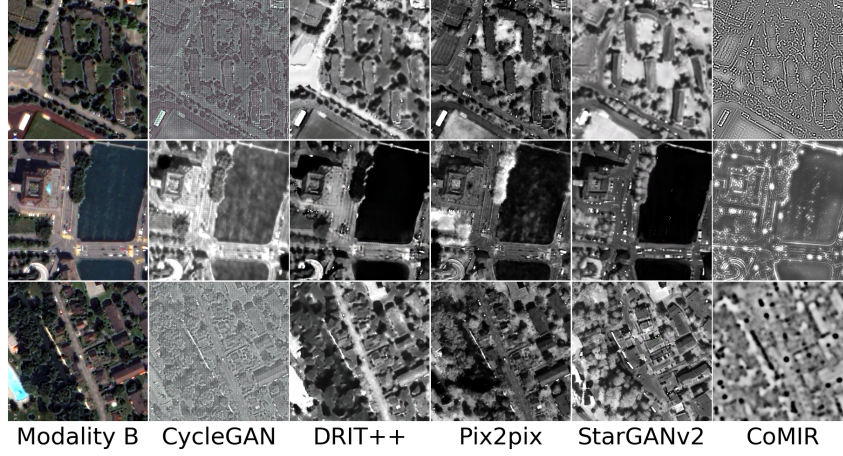
To complement these quantitative results, we show in Fig. 3–5 a few examples of modality-translated images, by the evaluated methods, for each of the observed datasets. The examples illustrate some of the above-commented behaviours of the different methods.

Figure 3 shows examples from the Zurich dataset, the easiest of the three, with a clear correlation between the observed modalities. All the observed I2I translation methods reach reasonable to very good results. *pix2pix* generates the most realistic images, in both directions; it not only preserves the structural information but also maps the local intensities as desired. This is also reflected in the low FID values in Table 1. Other examples point out some issues: CycleGAN is successful in translating Modality A to B, but not the other way around. DRIT++ preserves structures, but is less successful regarding intensity mapping, whereas StarGANv2 fails to preserve geometry (straight lines) and generates a number of (colourful) noise pixels.

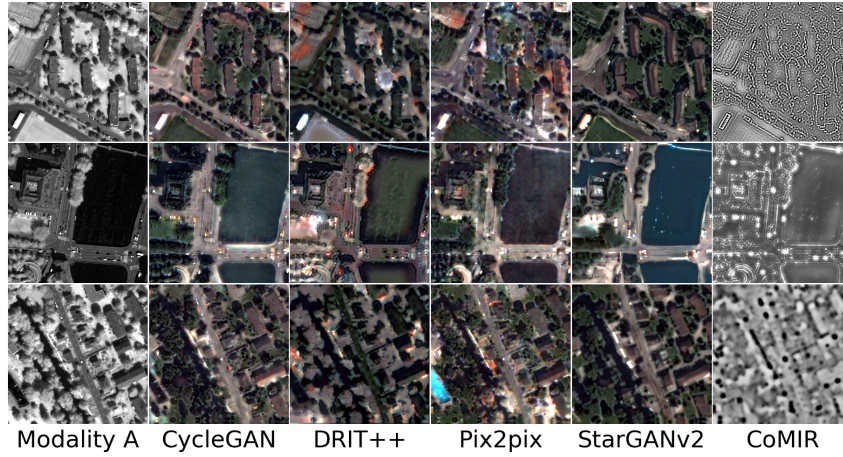
As can be seen in Fig. 4 and Fig. 5, all the I2I translation methods exhibit more or less degraded performance when applied to the more challenging biomedical datasets. Results on the Cytological dataset (Fig. 4) indicate that the performance depends a lot on the “direction” (as indicated by FID as well); while all the methods give reasonably good output when translating from Modality B to A, the quality when translating Modality A to B tends to be much lower. This is particularly visible for *pix2pix*.

The Histological dataset (Fig. 5), being the most challenging of the three, with distinctly different imaging modalities, elevates further issues and differences in the performance of the observed methods. Translated images exhibit non-realistic intensities and structures as well as “invented” details, particularly in translations from Modality A to B, where *pix2pix* completely fails. However, when instead translating from Modality B to A, *pix2pix* surprisingly captures the most structures, which is matched with the lowest FID value among the I2I methods on the Histological data.

We conclude that the visual assessment of the generated images most often supports the quantitative evaluation by FID, and clearly shows that none of the observed I2I translation methods exhibits stable performance, nor consistently outperforms the others. Even though we can not exclude the possibility that individually exploring the hyperparameter space and designing data augmenta-

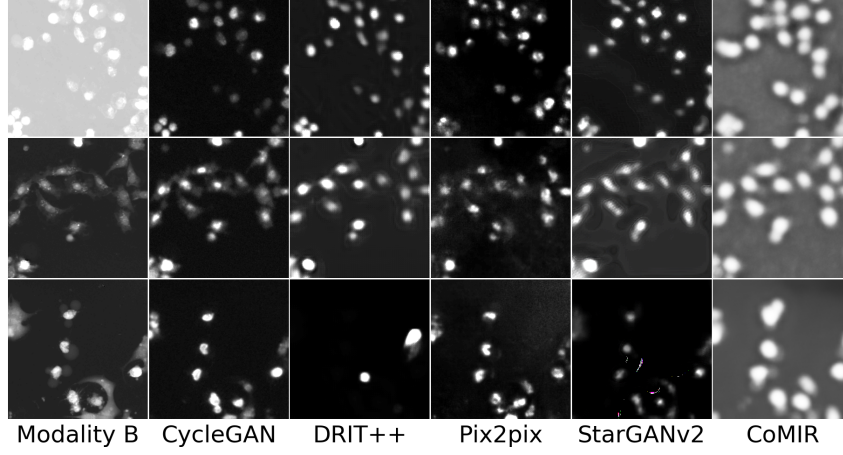


(a) Modality B to A: RGB images and their modality-translated results

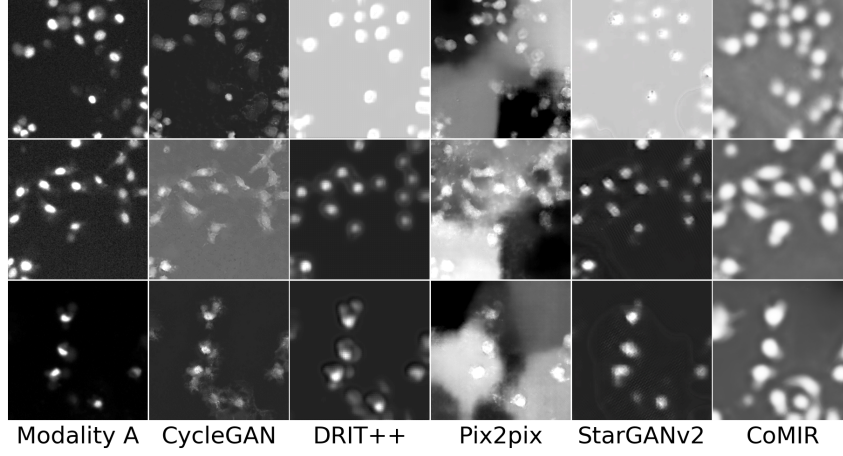


(b) Modality A to B: NIR images and their modality-translated results

Figure 3: Modality-transferred image samples of the Zurich dataset by different evaluated methods (contrast-enhanced for visualisation). Each row shows the results on one random image from each fold. (a) Generated from the image in the column Modality B, the remaining images should, row-wise, match the image in the column Modality A in (b). Similarly, the translated images in (b) should be compared, row-wise, with the corresponding image in the column Modality B in (a). The exception is CoMIR (the last columns), where instead the corresponding images in (a) and (b) should be as similar as possible.



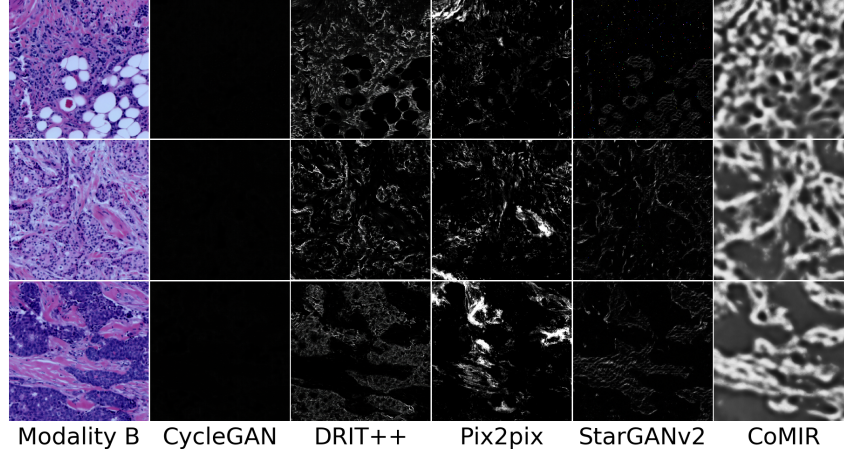
(a) Modality B to A: QPI images and their modality-translated results



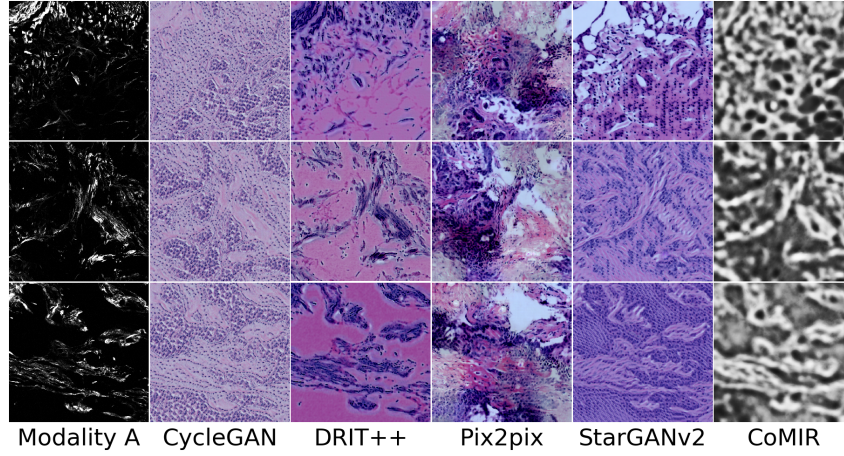
(b) Modality A to B: Fluorescence images and their modality-translated results

Figure 4: Modality-transferred image samples of the Cytological dataset by different evaluated methods (contrast-enhanced for visualisation). Each row shows the results on one random image from each fold. (a) Generated from the image in the column Modality B, the remaining images should, row-wise, match the image in the column Modality A in (b). Similarly, the translated images in (b) should be compared, row-wise, with the corresponding image in the column Modality B in (a). The exception is CoMIR (the last columns), where instead the corresponding images in (a) and (b) should be as similar as possible, being the learned representations of the two modalities.





(a) Modality B to A: BF images and their modality-translated results



(b) Modality A to B: SHG images and their modality-translated results

Figure 5: Modality-transferred image samples of the Histological dataset by different evaluated methods (contrast-enhanced for visualisation). Each row shows the results on one image randomly selected from the test set. (a) Generated from the image in the column Modality B, the remaining images should, row-wise, match the image in the column Modality A in (b). Similarly, the translated images in (b) should be compared, row-wise, with the corresponding image in the column Modality B in (a). The exception is CoMIR (the last columns), where instead the corresponding images in (a) and (b) should be as similar as possible, being the learned representations of the two modalities.

tion schemes for each I2I translation method could lead to its slightly improved performance, we believe that such changes would not affect our main conclusion.

Performance of CoMIR, the non-I2I (but rather representation learning) modality translation method, is visually evaluated by assessing the similarity of the corresponding learned representations. We observe relatively high similarity for all three datasets, while slightly decreasing with increasing modality differentiation exhibited from Zurich to Histological dataset, as also observed in the FID values.

## 6.2. Registration performance

Plots of registration success rate  $\lambda$  for increasing initial displacement  $d_{\text{Init}}$  for all the different evaluated combinations of methods are presented in Fig. 6. In Table 2, we summarise the aggregated performance, over all the considered displacements. A number of observations can be made from these results.

Reference performance is established by iterative MI maximisation (blue dashed line MI\_B2A). We observe that, for smaller initial displacements, MI maximisation delivers outstanding performance on all three datasets. However, it is also apparent that the performance of MI (optimised by adaptive stochastic gradient descent) decreases fast as the initial displacement increases. This is not surprising, since MI is known to have a small basin of attraction.

The yellow dash-dotted curve B2A indicates the performance of monomodal registration approaches (SIFT and  $\alpha$ -AMD, in the respective subplots), applied directly to multimodal images. As expected, these methods underperform MI maximisation in all cases except for SIFT on the Zurich dataset, for relatively large transformations.

The main focus of this study to analyse the positioning of the remaining (solid line) curves shown in Fig. 6, in comparison with the MI\_B2A and the B2A lines. First, we observe that, for each of the three datasets, there are a number of solid-line curves above the yellow dash-dotted curve B2A, for all observed displacements. This demonstrates that some I2I methods indeed can help to approach a “monomodal case”, and make the registration task easier when using the observed (monomodal) registration methods, SIFT and  $\alpha$ -AMD.

We also note that, similar as for the modality translation, the performances of the different registration methods show significant data-dependency. On the structure-rich Zurich data, SIFT performs rather well on modality translated images (and even on the original multimodal pairs). One exception is the StarGANv2 generated Zurich data, **star\_A** and **star\_B** in Fig. 6a and 6b, where SIFT is completely failing. On the biomedical data, where features are less salient,  $\alpha$ -AMD, being an intensity-based method, tends to come out ahead. Fig 6e particularly indicates very poor performance of SIFT-based registration on the Histological data.

In general, the I2I translation methods followed by either SIFT or  $\alpha$ -AMD registration appear as far less sensitive to the initial displacement, compared to MI; in particular, several of them outperform MI on Zurich dataset for larger displacements.





Figure 6: Success rate of the observed registration approaches. *x-axis*: initial displacement  $d_{\text{init}}$  between moving and fixed images, discretised into 10 equally sized bins (marked by vertical dotted lines). *y-axis*: success rate  $\lambda$  within each bin (averaged over 3 folds for Zurich and Cytological data). In the legend, *cyc*, *drit*, *p2p*, *star* and *comir* denote CycleGAN, DRIT++, pix2pix, StarGANv2, and CoMIR methods respectively. Suffix *\_A* (resp. *\_B*) denotes that generated Modality A (resp. B) is used for the (monomodal) registration. *B2A* denotes registration of the original multimodal images, without using any modality translation. *MI* and *CA* represent using MI maximisation and CurveAlign for registration, respectively.

Table 2: Overall registration success rate (in percent) for the evaluated methods on the three datasets. Larger is better. The success rate  $\lambda$  is aggregated over all transformation levels for each dataset. Standard deviations are taken over the 3 folds for Zurich and the Cytological data. *cyc*, *drit*, *p2p*, *star*, *comir*, MI and CA denote the methods CycleGAN, DRIT++, pix2pix, StarGANv2, CoMIR, MI maximisation and CurveAlign, respectively. *\_A* (resp. *\_B*) denotes using generated Modality A (resp. B) for registration. **B2A** refers to the multimodal registration performance on the acquired images without modality translation. **MI\_B2A** provides reference performance of a good conventional multimodal registration method. For each dataset, the best I2I-based approach, as well as the overall best performing (multimodal) approach, are bolded.

Dataset	Zurich Data		Cytological Data		Histological Data	
Method	$\alpha$ -AMD	SIFT	$\alpha$ -AMD	SIFT	$\alpha$ -AMD	SIFT
cyc_A	4.9 $\pm$ 2.1	66.4 $\pm$ 18.8	<b>71.1<math>\pm</math>5.8</b>	24.4 $\pm$ 6.2	0	0
cyc_B	65.0 $\pm$ 8.4	83.2 $\pm$ 3.1	19.2 $\pm$ 2.8	17.6 $\pm$ 2.5	13.8	0
drit_A	34.8 $\pm$ 5.4	38.0 $\pm$ 7.9	61.6 $\pm$ 16.2	21.6 $\pm$ 3.6	1.7	0
drit_B	18.1 $\pm$ 3.1	35.4 $\pm$ 3.5	21.0 $\pm$ 9.0	4.6 $\pm$ 1.3	4.7	0
p2p_A	80.2 $\pm$ 3.9	<b>98.3<math>\pm</math>0.5</b>	57.9 $\pm$ 7.4	8.6 $\pm$ 1.2	<b>28.4</b>	0
p2p_B	61.5 $\pm$ 4.7	85.0 $\pm$ 5.0	0.1 $\pm$ 0.1	3.8 $\pm$ 2.0	0.4	0
star_A	64.0 $\pm$ 7.5	6.5 $\pm$ 2.7	57.4 $\pm$ 13.0	10.9 $\pm$ 2.2	2.6	0
star_B	41.1 $\pm$ 3.6	5.9 $\pm$ 0.5	17.8 $\pm$ 4.9	5.8 $\pm$ 0.6	19.6	0
comir	91.8 $\pm$ 7.7	<b>100.0<math>\pm</math>0.0</b>	68.0 $\pm$ 14.0	72.5 $\pm$ 7.1	<b>81.3</b>	59.3
B2A	12.8 $\pm$ 3.5	72.5 $\pm$ 4.8	21.9 $\pm$ 10.5	20.8 $\pm$ 2.0	0	0
MI_B2A	69.1 $\pm$ 3.7		<b>89.9<math>\pm</math>3.0</b>		47.8	
CA_B2A					3.7	

What stands out in both Table 2 and in Fig. 6 is the CoMIR (representation learning-based) modality translation method. The combination of CoMIR and SIFT is the only one that does not fail on the Histological data, in Fig. 6e, while at the same time clearly outperforming the baseline for mid and large displacements. On the Histological dataset, CoMIR followed by  $\alpha$ -AMD is the clear winner, while on the Cytological data MI is taking the top position, followed by CoMIR combined with either SIFT or  $\alpha$ -AMD, or CycleGAN combined with  $\alpha$ -AMD. On the easier Zurich dataset, CoMIR performs best again, both when combined with SIFT (here the better of the two) and with  $\alpha$ -AMD.

Figures 6e and 6f also include the performance of the CurveAlign method, specially designed for registration of BF and SHG images in our Histological dataset. We observe that this method shows some limited success only for relatively small displacements, and falls behind MI and CoMIR, as well as several I2I translation methods when combined with  $\alpha$ -AMD.

### 6.3. Correlation between modality translation and registration

Intuitively, the more successful the modality translation is, the more accurate subsequent registration will be. Our results to a high extent confirm this: the observed performance of most combinations of methods is consistent with the appearance of the image samples in Fig. 3, Fig. 4 and Fig. 5. To visualise this consistency, we plot, in Fig. 7, the relation between overall success rate  $\lambda$ , for each of the observed combinations of modality translation and registration, and the average quality of the used modality translation, as quantified by FID, for

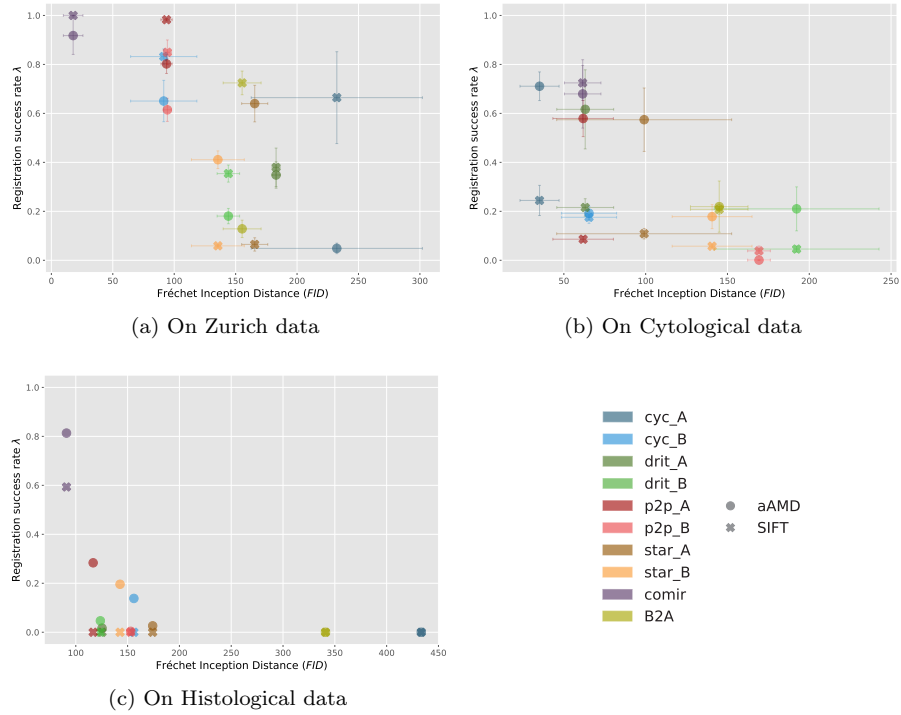


Figure 7: Relation between average FID reached by a modality translation method and the success rate  $\lambda$  of the subsequent registration. In the legend, *cyc*, *drit*, *p2p*, *star* and *comir* denote the methods CycleGAN, DRIT++, pix2pix, StarGANv2 and CoMIR, respectively. Suffix *\_A* (resp. *\_B*) denotes that generated Modality A (resp. B) is used in (monomodal) registration. The marker style indicates whether  $\alpha$ -AMD (aAMD) or SIFT (SIFT) is used for the registration. The error-bars correspond to standard deviation computed over 3 folds for Zurich and Cytological data.

the three observed datasets. In Fig 7a and 7b the error-bars show the standard deviations over the three folds of Zurich and Cytological datasets.

The results show a clear common trend that lower FID (higher quality of the generated image) generally correlates with higher registration success rate. The large error-bars, in particular for `cyc_A` in Fig. 7a and `drit_B` and `star_A` in Fig. 7b, indicate that the corresponding GAN-based methods are highly unstable in modality translation. Also here we observe that the difference in performance between the two directions of modality translation may be rather high. Whereas the two modalities in the Cytological dataset visually differ less than those in Zurich and the Histological datasets, our results (summarised in Fig. 7b) clearly show that all the four observed I2I translation methods have much more success in generating Modality A, than Modality B. This difference further propagates to registration, which is evidently more successful if based on generated Modality A, for both SIFT and  $\alpha$ -AMD.

#### 6.4. Overview of the results

The presented results allow for the following summary:

- The observed I2I translation methods, followed by monomodal registration approaches, show to be applicable in easier multimodal registration scenarios, but exhibit high instability and data dependence. The four observed I2I translation methods, with different properties and of different complexity, show varying performance on the observed datasets, including asymmetry w.r.t. to the direction of translation, without any of the methods standing out as a generally preferred choice.
- FID, as a measure of performance of I2I translation methods, shows to be a reasonably reliable predictor of the success of subsequent monomodal registration; I2I translation methods which manage to reach lower FID measured between the originally acquired and modality translated images can be expected to provide a better basis for a successful registration.
- Among the observed modality translation methods, `pix2pix` and `CoMIR` require aligned image pairs during training. These methods also show superior performance, in particular on the highly structured Zurich dataset, compared to the I2I translation methods which can be trained on non-aligned image pairs.
- The traditional registration approach based on MI maximisation exhibits excellent performance, leaving behind all the observed I2I methods for sufficiently small displacements. The combination of modality translation and monomodal registration, on the other hand, show better stability w.r.t. size of displacement.
- Several I2I translation methods followed by  $\alpha$ -AMD outperform a highly specialised method developed for registration of here observed Histological dataset.

- CoMIR, a representation-learning method developed for multimodal registration, exhibits overall best performance, showing stability w.r.t. data, size of displacement, as well as the choice of subsequent monomodal registration method.

## 7. Conclusion

In this study, we investigate whether and to what extent I2I translation methods may facilitate multimodal biomedical image registration. We focus on 2D rigid transformations, finding the task challenging enough, in particular for biomedical multimodal image data. We have selected four popular and widely used I2I translation methods with diverse properties and complexity. We believe that this selection gives a good insight into the potential of modality translation as a general approach to aid multimodal registration. Openly available multimodal biomedical datasets suitable for the evaluation of registration methods are very scarce. We use three datasets (two of them published in connection with this study) of varying complexity and different combinations of modalities, introducing a range of challenges relevant for performance evaluation.

From our experiments, we observe that I2I translation methods appear less successful in the context of multimodal registration than in some other relevant biomedical use-case scenarios (such as virtual staining, or image segmentation). However, a representation-learning approach (CoMIR), which maps the modalities to their established (learned) “common ground”, instead of mapping one of them all the way to the other, shows to be a highly promising approach which, we expect, will find applications and inspire further development.

This comparative study adds to the understanding of multimodal biomedical image registration methods from an empirical perspective. Last but not least, it establishes an open-source quantitative evaluation framework for multimodal biomedical registration based on publicly available datasets, which can be easily utilised for benchmarking, whereby we also hope to contribute to the openness and reproducibility of future scientific research.

## Acknowledgements

We thank Kevin Eliceiri (University of Wisconsin-Madison) and his team for kindly providing the data<sup>16</sup> used to create the Histological dataset. We thank Jaromír Gumulec (Masaryk University) and his collaborators for kindly providing the Cytological dataset<sup>17,18</sup>. We thank Michele Volpi and his collaborators for kindly providing the Zurich Summer Dataset. The authors are financially supported by the Wallenberg Autonomous Systems and Software Program, WASP, AI-Math initiative, VINNOVA (MedTech4Health project 2017-02447) and the Swedish Research Council (project 2017-04385).

<sup>16</sup><https://zenodo.org/record/4550300>

<sup>17</sup><https://zenodo.org/record/2601562>

<sup>18</sup><https://zenodo.org/record/4531900>

## References

- [1] A. Walter, P. Paul-Gilloteaux, B. Plochberger, L. Sefc, P. Verkade, J. G. Mannheim, P. Slezak, A. Unterhuber, M. Marchetti-Deschmann, M. Ogris, K. Bühler, D. Fixler, S. H. Geyer, W. J. Weninger, M. Glösmann, S. Handschuh, T. Wanek, Correlated Multimodal Imaging in Life Sciences: Expanding the Biomedical Horizon, *Front. Phys.* 8 (2020) 47. doi:10.3389/fphy.2020.00047.
- [2] L. G. Brown, A survey of image registration techniques, *ACM Comput. Surv.* 24 (4) (1992) 325–376. doi:10.1145/146370.146374.
- [3] B. Zitová, J. Flusser, Image registration methods: A survey, *Image and Vision Computing* 21 (11) (2003) 977–1000. doi:10.1016/S0262-8856(03)00137-9.
- [4] M. A. Viergever, J. A. Maintz, S. Klein, K. Murphy, M. Staring, J. P. Pluim, A survey of medical image registration – under review, *Medical Image Analysis* 33 (2016) 140–144. doi:10.1016/j.media.2016.06.030.
- [5] D. L. Hill, P. G. Batchelor, M. Holden, D. J. Hawkes, Medical image registration, *Phys Med Biol* 46 (3) (2001) R1–45. doi:10.1088/0031-9155/46/3/201.
- [6] G. Haskins, U. Kruger, P. Yan, Deep learning in medical image registration: A survey, *Machine Vision and Applications* 31 (1) (2020) 8. arXiv:1903.02026, doi:10.1007/s00138-020-01060-x.
- [7] Y. Fu, Y. Lei, T. Wang, W. J. Curran, T. Liu, X. Yang, Deep learning in medical image registration: A review, *Phys. Med. Biol.* 65 (20) (2020) 20TR01. arXiv:1912.12318, doi:10.1088/1361-6560/ab843e.
- [8] H. R. Boveiri, R. Khayami, R. Javidan, A. Mehdizadeh, Medical image registration using deep neural networks: A comprehensive review, *Computers & Electrical Engineering* 87 (2020) 106767. arXiv:2002.03401, doi:10.1016/j.compeleceng.2020.106767.
- [9] P. Isola, J.-Y. Zhu, T. Zhou, A. A. Efros, Image-To-Image Translation With Conditional Adversarial Networks, in: *Proceedings of the IEEE Conference on Computer Vision and Pattern Recognition*, 2017, pp. 1125–1134. doi:10.1109/CVPR.2017.632.
- [10] J.-Y. Zhu, T. Park, P. Isola, A. A. Efros, Unpaired Image-to-Image Translation Using Cycle-Consistent Adversarial Networks, in: *2017 IEEE International Conference on Computer Vision (ICCV)*, IEEE, Venice, 2017, pp. 2242–2251. doi:10.1109/ICCV.2017.244.
- [11] Y. Choi, Y. Uh, J. Yoo, J.-W. Ha, StarGAN v2: Diverse Image Synthesis for Multiple Domains, in: *2020 IEEE/CVF Conference on Computer Vision and Pattern Recognition (CVPR)*, IEEE, Seattle, WA, USA, 2020, pp. 8185–8194. doi:10.1109/CVPR42600.2020.00821.

- [12] H.-Y. Lee, H.-Y. Tseng, J.-B. Huang, M. Singh, M.-H. Yang, Diverse Image-to-Image Translation via Disentangled Representations, in: *Computer Vision – ECCV 2018*, Springer International Publishing, Cham, 2018, pp. 36–52.
- [13] H.-Y. Lee, H.-Y. Tseng, Q. Mao, J.-B. Huang, Y.-D. Lu, M. Singh, M.-H. Yang, DRIT++: Diverse Image-to-Image Translation via Disentangled Representations, *Int J Comput VisarXiv:1905.01270*, doi:10.1007/s11263-019-01284-z.
- [14] M. E. Tschuchnig, G. J. Oostingh, M. Gadermayr, Generative Adversarial Networks in Digital Pathology: A Survey on Trends and Future Potential, *Patterns* 1 (6) (2020) 100089. doi:10.1016/j.patter.2020.100089.
- [15] E. Meijering, A bird’s-eye view of deep learning in bioimage analysis, *Comput Struct Biotechnol J* 18 (2020) 2312–2325. doi:10.1016/j.csbj.2020.08.003.
- [16] W. M. Wells III, P. Viola, H. Atsumi, S. Nakajima, R. Kikinis, Multi-modal volume registration by maximization of mutual information, *Medical image analysis* 1 (1) (1996) 35–51.
- [17] F. Maes, A. Collignon, D. Vandermeulen, G. Marchal, P. Suetens, Multi-modality image registration by maximization of mutual information, *IEEE transactions on Medical Imaging* 16 (2) (1997) 187–198.
- [18] A. Keikhosravi, B. Li, Y. Liu, K. W. Eliceiri, Intensity-based registration of bright-field and second-harmonic generation images of histopathology tissue sections, *Biomed. Opt. Express* 11 (1) (2020) 160. doi:10.1364/BOE.11.000160.
- [19] N. Pielawski, E. Wetzer, J. Öfverstedt, J. Lu, C. Wählby, J. Lindblad, N. Sladoje, CoMIR: Contrastive multimodal image representation for registration, in: *Advances in Neural Information Processing Systems*, Vol. 33, Curran Associates, Inc., 2020, pp. 18433–18444. arXiv:2006.06325.
- [20] C. Studholme, D. L. Hill, D. J. Hawkes, An overlap invariant entropy measure of 3D medical image alignment, *Pattern recognition* 32 (1) (1999) 71–86.
- [21] J. P. Pluim, J. A. Maintz, M. A. Viergever, Image registration by maximization of combined mutual information and gradient information, in: *International Conference on Medical Image Computing and Computer-Assisted Intervention*, Springer, 2000, pp. 452–461.
- [22] J. Öfverstedt, J. Lindblad, N. Sladoje, Fast and Robust Symmetric Image Registration Based on Distances Combining Intensity and Spatial Information, *IEEE Trans. on Image Process.* 28 (7) (2019) 3584–3597. arXiv:1807.11599, doi:10.1109/TIP.2019.2899947.

- [23] X. Yang, R. Kwitt, M. Styner, M. Niethammer, Quicksilver: Fast predictive image registration – A deep learning approach, *NeuroImage* 158 (2017) 378–396. doi:10.1016/j.neuroimage.2017.07.008.
- [24] X. Cheng, L. Zhang, Y. Zheng, Deep similarity learning for multimodal medical images, *Computer Methods in Biomechanics and Biomedical Engineering: Imaging & Visualization* 6 (3) (2018) 248–252. doi:10.1080/21681163.2015.1135299.
- [25] G. Balakrishnan, A. Zhao, M. R. Sabuncu, J. Guttag, A. V. Dalca, VoxelMorph: A Learning Framework for Deformable Medical Image Registration, *IEEE Transactions on Medical Imaging* 38 (8) (2019) 1788–1800. doi:10.1109/TMI.2019.2897538.
- [26] D. Lowe, Object recognition from local scale-invariant features, in: *Proceedings of the Seventh IEEE International Conference on Computer Vision*, Vol. 2, 1999, pp. 1150–1157 vol.2. doi:10.1109/ICCV.1999.790410.
- [27] E. Rublee, V. Rabaud, K. Konolige, G. Bradski, ORB: An efficient alternative to SIFT or SURF, in: *2011 International Conference on Computer Vision*, IEEE, Barcelona, Spain, 2011, pp. 2564–2571. doi:10.1109/ICCV.2011.6126544.
- [28] G. Wu, M. Kim, Q. Wang, Y. Gao, S. Liao, D. Shen, Unsupervised Deep Feature Learning for Deformable Registration of MR Brain Images, in: *Medical Image Computing and Computer-Assisted Intervention – MICCAI 2013*, Lecture Notes in Computer Science, Springer Berlin Heidelberg, 2013, pp. 649–656.
- [29] A. Dosovitskiy, J. T. Springenberg, M. Riedmiller, T. Brox, Discriminative unsupervised feature learning with convolutional neural networks, in: *Proceedings of the 27th International Conference on Neural Information Processing Systems - Volume 1*, NIPS’14, MIT Press, Cambridge, MA, USA, 2014, pp. 766–774.
- [30] M. P. Heinrich, M. Jenkinson, M. Bhushan, T. Martin, F. V. Gleeson, S. M. Brady, J. A. Schnabel, MIND: Modality independent neighbourhood descriptor for multi-modal deformable registration, *Med Image Anal* 16 (7) (2012) 1423–1435. doi:10.1016/j.media.2012.05.008.
- [31] C. Qin, B. Shi, R. Liao, T. Mansi, D. Rueckert, A. Kamen, Unsupervised Deformable Registration for Multi-modal Images via Disentangled Representations, in: *Information Processing in Medical Imaging*, Lecture Notes in Computer Science, Springer International Publishing, 2019, pp. 249–261.
- [32] I. J. Goodfellow, J. Pouget-Abadie, M. Mirza, B. Xu, D. Warde-Farley, S. Ozair, A. Courville, Y. Bengio, Generative adversarial nets, in: *Proceedings of the 27th International Conference on Neural Information Processing Systems - Volume 2*, NIPS’14, MIT Press, Cambridge, MA, USA, 2014, pp. 2672–2680.



- [33] Y. Rivenson, H. Wang, Z. Wei, K. de Haan, Y. Zhang, Y. Wu, H. Günaydin, J. E. Zuckerman, T. Chong, A. E. Sisk, L. M. Westbrook, W. D. Wallace, A. Ozcan, Virtual histological staining of unlabelled tissue-autofluorescence images via deep learning, *Nat Biomed Eng* 3 (6) (2019) 466–477. doi:10.1038/s41551-019-0362-y.
- [34] T. de Bel, M. Hermesen, J. Kers, J. van der Laak, G. Litjens, Stain-transforming cycle-consistent generative adversarial networks for improved segmentation of renal histopathology, in: *Proceedings of the 2nd International Conference on Medical Imaging with Deep Learning*, Vol. 102 of *Proceedings of Machine Learning Research*, PMLR, London, United Kingdom, 2019, pp. 151–163.
- [35] E. A. Burlingame, A. A. Margolin, J. W. Gray, Y. H. Chang, SHIFT: Speedy histopathological-to-immunofluorescent translation of whole slide images using conditional generative adversarial networks, in: *Medical Imaging 2018: Digital Pathology*, Vol. 10581, International Society for Optics and Photonics, 2018, p. 1058105. doi:10.1117/12.2293249.
- [36] M. M. R. Siddiquee, Z. Zhou, N. Tajbakhsh, R. Feng, M. Gotway, Y. Bengio, J. Liang, Learning Fixed Points in Generative Adversarial Networks: From Image-to-Image Translation to Disease Detection and Localization, in: *2019 IEEE/CVF International Conference on Computer Vision (ICCV)*, IEEE, Seoul, Korea (South), 2019, pp. 191–200. doi:10.1109/ICCV.2019.00028.
- [37] K. Armanious, C. Jiang, S. Abdulatif, T. Kustner, S. Gatidis, B. Yang, Unsupervised Medical Image Translation Using Cycle-MedGAN, in: *2019 27th European Signal Processing Conference (EUSIPCO)*, IEEE, A Coruna, Spain, 2019, pp. 1–5. doi:10.23919/EUSIPCO.2019.8902799.
- [38] S. Engelhardt, R. De Simone, P. M. Full, M. Karck, I. Wolf, Improving Surgical Training Phantoms by Hyperrealism: Deep Unpaired Image-to-Image Translation from Real Surgeries, in: *Medical Image Computing and Computer Assisted Intervention – MICCAI 2018*, Vol. 11070, Springer International Publishing, Cham, 2018, pp. 747–755. doi:10.1007/978-3-030-00928-1\_84.
- [39] X. Cao, J. Yang, Y. Gao, Y. Guo, G. Wu, D. Shen, Dual-core steered non-rigid registration for multi-modal images via bi-directional image synthesis, *Medical image analysis* 41 (2017) 18–31.
- [40] M. Arar, Y. Ginger, D. Danon, A. H. Bermano, D. Cohen-Or, Unsupervised Multi-Modal Image Registration via Geometry Preserving Image-to-Image Translation, in: *2020 IEEE/CVF Conference on Computer Vision and Pattern Recognition (CVPR)*, IEEE, Seattle, WA, USA, 2020, pp. 13407–13416. doi:10.1109/CVPR42600.2020.01342.

- [41] D. Mahapatra, B. Antony, S. Sedai, R. Garnavi, Deformable medical image registration using generative adversarial networks, in: 2018 IEEE 15th International Symposium on Biomedical Imaging (ISBI 2018), IEEE, Washington, DC, 2018, pp. 1449–1453. doi:10.1109/ISBI.2018.8363845.
- [42] A. Sheikhjafari, M. Noga, K. Punithakumar, N. Ray, Unsupervised deformable image registration with fully connected generative neural network, in: International Conference on Medical Imaging with Deep Learning (MIDL), Amsterdam, The Netherlands, 2018.
- [43] S. Kaji, S. Kida, Overview of image-to-image translation by use of deep neural networks: Denoising, super-resolution, modality conversion, and reconstruction in medical imaging, Radiol Phys Technol 12 (3) (2019) 235–248. doi:10.1007/s12194-019-00520-y.
- [44] Y. Pang, J. Lin, T. Qin, Z. Chen, Image-to-Image Translation: Methods and Applications, arXiv:2101.08629 [cs]arXiv:2101.08629.
- [45] A. V. Dalca, G. Balakrishnan, J. Guttag, M. R. Sabuncu, Unsupervised Learning for Fast Probabilistic Diffeomorphic Registration, in: Medical Image Computing and Computer Assisted Intervention – MICCAI 2018, Lecture Notes in Computer Science, Springer International Publishing, Cham, 2018, pp. 729–738. doi:10.1007/978-3-030-00928-1\_82.
- [46] B. D. de Vos, F. F. Berendsen, M. A. Viergever, H. Sokootti, M. Staring, I. Išgum, A deep learning framework for unsupervised affine and deformable image registration, Medical Image Analysis 52 (2019) 128–143. doi:10.1016/j.media.2018.11.010.
- [47] H. Jiang, H. Yu, X. Zhou, H. Kang, Z. Wang, T. Hara, H. Fujita, Learning 3D non-rigid deformation based on an unsupervised deep learning for PET/CT image registration, in: Medical Imaging 2019: Biomedical Applications in Molecular, Structural, and Functional Imaging, SPIE, San Diego, United States, 2019, p. 67. doi:10.1117/12.2512698.
- [48] M. Mirza, S. Osindero, Conditional generative adversarial nets, arXiv preprint arXiv:1411.1784arXiv:1411.1784.
- [49] O. Ronneberger, P. Fischer, T. Brox, U-Net: Convolutional Networks for Biomedical Image Segmentation, in: Medical Image Computing and Computer-Assisted Intervention – MICCAI 2015, Lecture Notes in Computer Science, Springer International Publishing, 2015, pp. 234–241.
- [50] T.-C. Wang, M.-Y. Liu, J.-Y. Zhu, A. Tao, J. Kautz, B. Catanzaro, High-Resolution Image Synthesis and Semantic Manipulation with Conditional GANs, in: 2018 IEEE/CVF Conference on Computer Vision and Pattern Recognition, IEEE, Salt Lake City, UT, USA, 2018, pp. 8798–8807. doi:10.1109/CVPR.2018.00917.

- [51] P. Zhang, B. Zhang, D. Chen, L. Yuan, F. Wen, Cross-Domain Correspondence Learning for Exemplar-Based Image Translation, in: 2020 IEEE/CVF Conference on Computer Vision and Pattern Recognition (CVPR), IEEE, Seattle, WA, USA, 2020, pp. 5142–5152. doi:10.1109/CVPR42600.2020.00519.
- [52] Y. Taigman, A. Polyak, L. Wolf, Unsupervised Cross-Domain Image Generation, arXiv:1611.02200 [cs]arXiv:1611.02200.
- [53] T. Kim, M. Cha, H. Kim, J. K. Lee, J. Kim, Learning to Discover Cross-Domain Relations with Generative Adversarial Networks, in: International Conference on Machine Learning, PMLR, 2017, pp. 1857–1865.
- [54] Z. Yi, H. Zhang, P. Tan, M. Gong, DualGAN: Unsupervised Dual Learning for Image-to-Image Translation, in: 2017 IEEE International Conference on Computer Vision (ICCV), IEEE, Venice, 2017, pp. 2868–2876. doi:10.1109/ICCV.2017.310.
- [55] T. de Bel, J.-M. Bokhorst, J. van der Laak, G. Litjens, Residual cyclegan for robust domain transformation of histopathological tissue slides, Medical Image Analysis 70 (2021) 102004. doi:10.1016/j.media.2021.102004.
- [56] M.-Y. Liu, T. Breuel, J. Kautz, Unsupervised image-to-image translation networks, in: Proceedings of the 31st International Conference on Neural Information Processing Systems, NIPS’17, Curran Associates Inc., Long Beach, California, USA, 2017, pp. 700–708.
- [57] Q. Mao, H.-Y. Lee, H.-Y. Tseng, S. Ma, M.-H. Yang, Mode Seeking Generative Adversarial Networks for Diverse Image Synthesis, in: 2019 IEEE/CVF Conference on Computer Vision and Pattern Recognition (CVPR), IEEE, Long Beach, CA, USA, 2019, pp. 1429–1437. arXiv:1903.05628, doi:10.1109/CVPR.2019.00152.
- [58] R. D. Hjelm, A. Fedorov, S. Lavoie-Marchildon, K. Grewal, P. Bachman, A. Trischler, Y. Bengio, Learning deep representations by mutual information estimation and maximization, in: International Conference on Learning Representations, 2018. arXiv:1808.06670.
- [59] J. Lindblad, N. Sladoje, Linear Time Distances Between Fuzzy Sets With Applications to Pattern Matching and Classification, IEEE Trans. on Image Process. 23 (1) (2014) 126–136. doi:10.1109/TIP.2013.2286904.
- [60] L. Solorzano, C. Pereira, D. Martins, R. Almeida, F. Carneiro, G. M. Almeida, C. Oliveira, C. Wahlby, Towards Automatic Protein Co-Expression Quantification in Immunohistochemical TMA Slides, IEEE J. Biomed. Health Inform. 25 (2) (2021) 393–402. doi:10.1109/JBHI.2020.3008821.
- [61] M. Volpi, V. Ferrari, Semantic segmentation of urban scenes by learning local class interactions, in: 2015 IEEE Conference on Computer Vision and

- Pattern Recognition Workshops (CVPRW), 2015, pp. 1–9. doi:10.1109/CVPRW.2015.7301377.
- [62] T. Vicar, M. Raudenska, J. Gumulec, J. Balvan, The Quantitative-Phase Dynamics of Apoptosis and Lytic Cell Death, *Scientific Reports* 10 (1) (2020) 1–12. doi:10.1038/s41598-020-58474-w.
  - [63] T. Vicar, M. Raudenska, J. Gumulec, M. Masarik, J. Balvan, Fluorescence microscopy timelapse dataset of PNT1A, DU-145 and LNCaP cells with annotated caspase 3,7-dependent and independent cell death (Feb. 2021). doi:10.5281/ZENODO.4531900.
  - [64] T. Vicar, M. Raudenska, J. Gumulec, M. Masarik, J. Balvan, Quantitative phase microscopy timelapse dataset of PNT1A, DU-145 and LNCaP cells with annotated caspase 3,7-dependent and independent cell death (Mar. 2019). doi:10.5281/ZENODO.2601562.
  - [65] K. Eliceiri, B. Li, A. Keikhosravi, Multimodal Biomedical Dataset for Evaluating Registration Methods (Full-size TMA Cores) (Feb. 2021). doi:10.5281/ZENODO.4550300.
  - [66] K. Marstal, F. Berendsen, M. Staring, S. Klein, SimpleElastix: A User-Friendly, Multi-Lingual Library for Medical Image Registration, in: *Proceedings of the IEEE Conference on Computer Vision and Pattern Recognition Workshops*, 2016, pp. 134–142.
  - [67] S. Klein, J. P. W. Pluim, M. Staring, M. A. Viergever, Adaptive Stochastic Gradient Descent Optimisation for Image Registration, *Int J Comput Vis* 81 (3) (2008) 227. doi:10.1007/s11263-008-0168-y.
  - [68] G. Bradski, The OpenCV library, *Dr. Dobb’s Journal of Software Tools*.
  - [69] M. A. Fischler, R. C. Bolles, Random sample consensus: A paradigm for model fitting with applications to image analysis and automated cartography, *Commun. ACM* 24 (6) (1981) 381–395. doi:10.1145/358669.358692.
  - [70] S. van der Walt, J. L. Schönberger, J. Nunez-Iglesias, F. Boulogne, J. D. Warner, N. Yager, E. Gouillart, T. Yu, Scikit-image: Image processing in Python, *PeerJ* 2 (2014) e453. doi:10.7717/peerj.453.
  - [71] M. Heusel, H. Ramsauer, T. Unterthiner, B. Nessler, S. Hochreiter, GANs Trained by a Two Time-Scale Update Rule Converge to a Local Nash Equilibrium, in: *Advances in Neural Information Processing Systems*, Vol. 30, 2017, pp. 6626–6637.